

Phase-retrieved pupil functions in wide-field fluorescence microscopy

B. M. HANSER*‡, M. G. L. GUSTAFSSON†§, D. A. AGARD† & J. W. SEDAT†

*Graduate Group in Biophysics, and †Department of Biochemistry and Biophysics, University of California San Francisco, San Francisco, CA 94143-2240, U.S.A.

Key words. Deconvolution, fluorescence microscopy, phase retrieval, PSF, spherical aberration.

Summary

Pupil functions are compact and modifiable descriptions of the three-dimensional (3D) imaging properties of wide-field optical systems. The pupil function of a microscope can be computationally estimated from the measured point spread function (PSF) using phase retrieval algorithms. The compaction of a 3D PSF into a 2D pupil function suppresses artefacts and measurement noise without resorting to rotational averaging. We show here that such 'phase-retrieved' pupil functions can reproduce features in the optical path, both near the sample and in the microscope. Unlike the PSF, the pupil function can be easily modified to include known aberrations, such as those induced by index-mismatched mounting media, simply by multiplying the pupil function by a calculated aberration function. PSFs calculated from such a modified pupil function closely match the corresponding measured PSFs collected under the aberrated imaging conditions. When used for image deconvolution of simulated objects, these phase-retrieved, calculated PSFs perform similarly to directly measured PSFs.

Introduction

As modern microscopy develops into a more and more quantitative science, it is becoming increasingly essential to quantify the precise, three-dimensional (3D) imaging properties of each microscope. Such quantification is needed for accurate measurements, for advanced image processing including deconvolution, and for analysis and verification of system

performance. The most commonly used form of quantitative description is the intensity point spread function (PSF). However, the PSF is an inflexible description that describes only a single set of imaging conditions, namely those under which the PSF was measured. This is a major problem, as the imaging conditions encountered in practical biological microscopy vary widely and are rarely ideal. There is therefore a need for an alternative, flexible microscope description that can adapt to changing imaging conditions.

The PSF is a measure of the optical system's response to a point source and describes how every point in the original object $o(x,y,z)$ is blurred by the imaging system to produce the resulting observed intensity image $i(x,y,z)$. If the PSF can be assumed to be spatially invariant – every point in the object is blurred by the same PSF – the blurring takes the form of a convolution:

$$i = o \otimes \text{PSF} \quad (1)$$

where \otimes represents the convolution operator. This concept has led to the development of computational deconvolution methods, which attempt to solve Eq. (1) for the unknown object based on measurements of the image and the PSF of the imaging system (Agard *et al.*, 1989). PSFs for fluorescence microscopy have been produced either through theoretical calculations (McCutchen, 1964; Goodman, 1968; Gibson & Lanni, 1991; Visser & Wiersma, 1991; Philip, 1999), or by experimental measurement of the intensity PSF using a subresolution fluorescent object (Agard *et al.*, 1989; Hiraoka *et al.*, 1990). Any one PSF for a microscope describes its imaging properties only under the specific conditions under which it was measured. To be able to process data acquired under aberrated conditions, one must acquire multiple PSFs, each representing a particular degree of aberration (Scalettar *et al.*, 1996).

Theoretical PSFs have advantages in that they are noise-free, and in that known aberrations are easily included into the

Correspondence to: Professor J. W. Sedat. Tel.: +415 476 2489; fax: +415 476 1902; e-mail: sedat@msg.ucsf.edu

Present addresses: ‡Biological Imaging Center, Caltech, 139–74, 1200 E California Blvd., Pasadena, CA 91125, U.S.A.; §Department of Physiology and Division of Bioengineering, University of California San Francisco, San Francisco, CA 94143–2240, U.S.A.

calculations: both refractive index mismatch (Gibson & Lanni, 1991; Visser & Wiersma, 1991; Török *et al.*, 1995) and more complex spatially varying sample-induced aberrations (Kam *et al.*, 2001) have been incorporated. However, theoretical PSF calculations cannot take into account the specific properties of a particular microscope system, for instance imperfections due to manufacturing tolerances.

In contrast to theoretical PSFs, experimentally measured PSFs automatically include the individual features of the microscope system (Hiraoka *et al.*, 1990). This includes effects that are usually ignored by theoretical treatments, such as microscope- and objective-lens-specific aberrations that break the axial and rotational symmetry of the intensity PSF. However, the information on rotational asymmetry is lost if the measured PSF is rotationally averaged, as is often done to suppress noise. A measured intensity PSF represents only the specific conditions under which it was acquired, and cannot be modified. Thus a separate measured PSF is needed for each set of imaging conditions.

Another means for quantifying imaging properties is the intensity optical transfer function (OTF), which describes the frequency response of the optical system. The PSF and OTF are each other's Fourier transforms, and thus contain exactly the same information. The OTF therefore shares the same drawbacks as the PSF.

There is, however, a third way to specify the properties of an imaging system, namely through the pupil function, which is effectively a description of the magnitude and phase of the wavefront that a point source in the sample produces at the exit pupil of the imaging system. An important advantage of the pupil function description is that it is modifiable: theoretically calculated aberrations can be easily combined with a microscope-specific pupil function, which can then produce intensity PSFs that contain both these aberrations and the microscope-specific information (Hanser *et al.*, 2001).

The relationships between the PSF, the OTF and the pupil function are illustrated in Fig. 1. The intensity PSF (Fig. 1A) is the magnitude squared of a complex-valued amplitude PSF (PSF_A, Fig. 1B, also known as the coherent point spread function (Goodman, 1968)). The Fourier transform (FT) of the PSF_A is the complex-valued amplitude optical transfer function (OTF_A, also known as the 3D coherent OTF or generalized aperture (Fig. 1C, McCutchen, 1964)). The OTF_A is non-zero only on a 2D surface (a spherical cap), and its values can therefore be described by a 2D function: the pupil function. The intensity OTF (Fig. 1D) is the autocorrelation of the amplitude OTF, as well as being the Fourier transform of the intensity PSF.

The PSF and OTF can be easily interconverted mathematically through a 3D Fourier transform, and the same is true of PSF_A and OTF_A, but neither the magnitude-squared operation that converts PSF_A into PSF nor the autocorrelation that forms OTF from OTF_A can be directly inverted. This unidirectionality, illustrated by the vertical one-way arrows in Fig. 1,

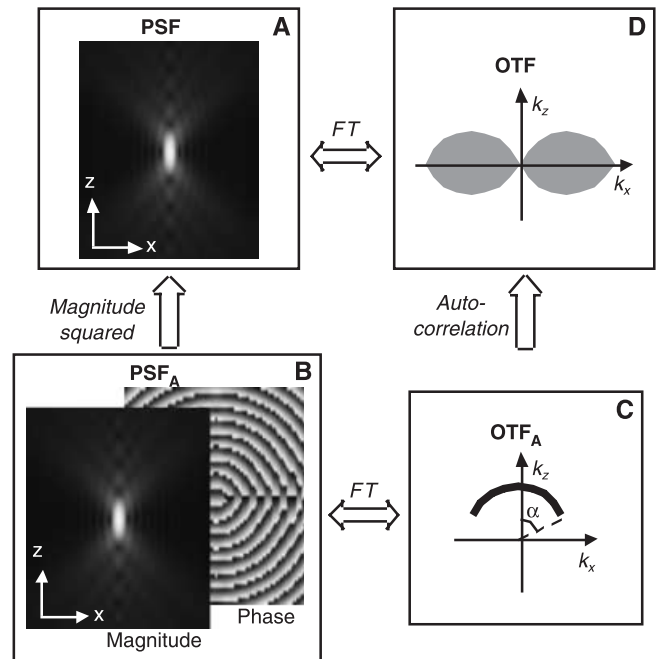


Fig. 1. The relationships between different ways to quantify 3D imaging properties. The measured intensity PSF (A) is the squared magnitude of a complex-valued amplitude PSF, the PSF_A, which contains phase as well as magnitude information (B). The Fourier transform (FT) of the PSF_A is the amplitude optical transfer function (OTF_A, C), which is non-zero only on a 2D surface that forms part of a spherical shell. The intensity OTF generally used in image processing (D) is the autocorrelation of the pupil function, and is also the FT of the intensity PSF. The pupil function (not shown) is the projection of the OTF_A onto the lateral (k_x, k_y) plane.

stems from the loss of phase information when the intensity is produced as the squared magnitude of the complex amplitude. It is therefore not trivial to determine the pupil function of a given imaging system, even though the intensity PSF is simple to measure.

Pupil functions of objective lenses can be measured directly (Zhou & Sheppard, 1997; Neil *et al.*, 1998; Beverage *et al.*, 2002), but this requires additional hardware, such as interferometers, which is impractical to implement for an existing microscope. However, indirect information about the pupil function is available in the easily measured intensity PSF. The problem of reconstructing the pupil function from intensity PSF data – the ‘phase retrieval’ problem – has been studied extensively in astronomy, and algorithms have been developed for this purpose (Gonsalves, 1982; Fienup, 1993; Lyon *et al.*, 1997; Luke *et al.*, 2002). Through phase retrieval, the pupil function can be estimated without requiring any additional optical equipment. These algorithms were originally developed for the exceedingly low numerical aperture (NA) of astronomical telescopes, but recently a modified method has been published that allows phase retrieval on high-NA systems such as high-resolution microscopes (Hanser *et al.*, 2003).

In this article, we demonstrate the use of phase-retrieved pupil functions to quantify the imaging properties of wide-field fluorescence microscopes. We use the phase retrieval algorithm of Hanser *et al.* (2003) to produce an estimate of the pupil function from a measured 3D intensity PSF, and calculate a reconstructed PSF (a 'phase-retrieved PSF') from the pupil function. We show that the resulting pupil function can model objects and aberrations in the optical path, both near the sample and in the back focal plane of the microscope. We then demonstrate how the pupil function can be easily modified by a calculated aberration function to reproduce accurately the features of PSFs measured under the aberrated imaging conditions. As an example, we show that modified, phase-retrieved PSFs match measured PSFs imaged deep in a mounting medium that does not have the appropriate refractive index for the objective lens. Finally, we test how PSFs calculated from these pupil functions perform for deconvolution, and show that their performance is similar to that of measured PSFs, and superior to that of rotationally averaged or purely theoretical PSFs.

Materials and methods

Sample preparation

PSFs were collected using slides of subresolution fluorescent beads prepared as follows (Hiraoka *et al.*, 1990): red fluorescent polystyrene beads (Fluospheres, 0.121 μm nominal diameter, Molecular Probes) were diluted in 95% ethanol. A 5–10- μL aliquot of the diluted bead solution was allowed to evaporate on a heated #1.5 cover glass and mounted in glycerol containing 3% n-propyl gallate. To avoid unintentional sample motion, the cover glass was rigidly affixed to a glass slide using clear nail polish.

To be able to compare measured and calculated index-mismatch aberrations, it was necessary to acquire PSFs using beads located at a variety of well-characterized depths below the cover slip. For this purpose, beads were applied as described above onto a support ball (1-mm-diameter sapphire ball lens, Edmund Industrial Optics, Barrington, NJ, U.S.A.) immobilized in near contact with the cover glass surface (see schematic in Fig. 12). The space between the support ball and the cover glass was filled with water.

Instrumentation and data collection

Data were collected on a Zeiss Axiomat inverted microscope fitted with a 100 \times /1.3NA oil-immersion Plan-Apochromat objective lens, a 16-bit liquid nitrogen-cooled CCD camera (UCSF/Photometrics), and a high-precision motorized *xyz* stage. The lateral pixel size was equivalent to 0.0566 μm in sample space, smaller than is required for Nyquist sampling. The emission filter bandpass was 610–670 nm; most of the emission of the Fluospheres occurs in the shorter-wavelength part of this band.

Three-dimensional PSF datasets were collected on the fluorescent bead samples by acquiring a series of 2D images (sections) with different defocus (Agard, 1984). The PSF datasets were collected either with a constant exposure time, or with longer exposure times for the far out-of-focus sections ('stepped exposure time') to improve their signal-to-noise ratio. The datasets were preprocessed to fix bad pixels, subtract background intensity and normalize for intensity variations due to lamp flicker, etc. A subset of the sections, usually four sections axially offset by approximately -3 , -1 , $+1$ and $+3$ μm from the peak intensity section, were selected for use in the phase retrieval.

To determine the depth of each bead in the support ball set-up described above, we measured the lateral distance of the bead from the centre of the ball, and the axial distance, if any, between the ball and the cover glass. Together with the known ball diameter, these measurements determine the bead depth. The lateral position of the ball centre could be located precisely by imaging the ball in the reflected-light mode of the microscope and observing the interference (Newton's rings) between light reflected off the ball and off the cover glass surface – these rings are laterally concentric with the ball. The lateral distance from that centre position to each bead was then determined with the help of the high-precision *xyz* stage. The axial distance of the ball from the cover glass was determined by observing small contaminant particles on the ball and cover glass, and the image of the closed-down field diaphragm reflected off the ball and cover glass surfaces. This small axial distance was corrected for optical distortions using a Zernike-based correction factor (Booth *et al.*, 1998).

Imaging model

The imaging model used in this paper has been described in Hanser *et al.* (2003). The intensity PSF of a wide-field fluorescence microscope is considered as the squared magnitude of a complex-valued amplitude point spread function, PSF_A , also known as the coherent point spread function (Goodman, 1968). The PSF_A is the 3D Fourier transform of an amplitude optical transfer function that is non-zero only on a spherical shell cap that has a radius n/λ and is angularly limited by the aperture angle α (Fig. 1C). Because the shell is a 2D, that 3D Fourier transform integral can be rewritten as a 2D integral of a pupil function $P(k_x, k_y)$ over a 2D circular pupil that is the projection of the shell onto the k_x, k_y plane. The spherical shape of the shell is accounted for separately by expressing k_z as a function of k_x and k_y :

$$\text{PSF}_A(x, y, z) = \iint_{\text{pupil}} P(k_x, k_y) e^{2\pi i(k_x x + k_y y)} e^{2\pi i k_z(k_x, k_y) z} d_{k_x} d_{k_y}. \quad (2)$$

The explicit form of $k_z(k_x, k_y)$ is $k_z(k_x, k_y) = \sqrt{[(n/\lambda)^2 - (k_x^2 + k_y^2)]}$, where λ is the wavelength of the observation light, and n the refractive index of the immersion medium. Both P and PSF_A are complex quantities, and the integral in Eq. (2) is evaluated

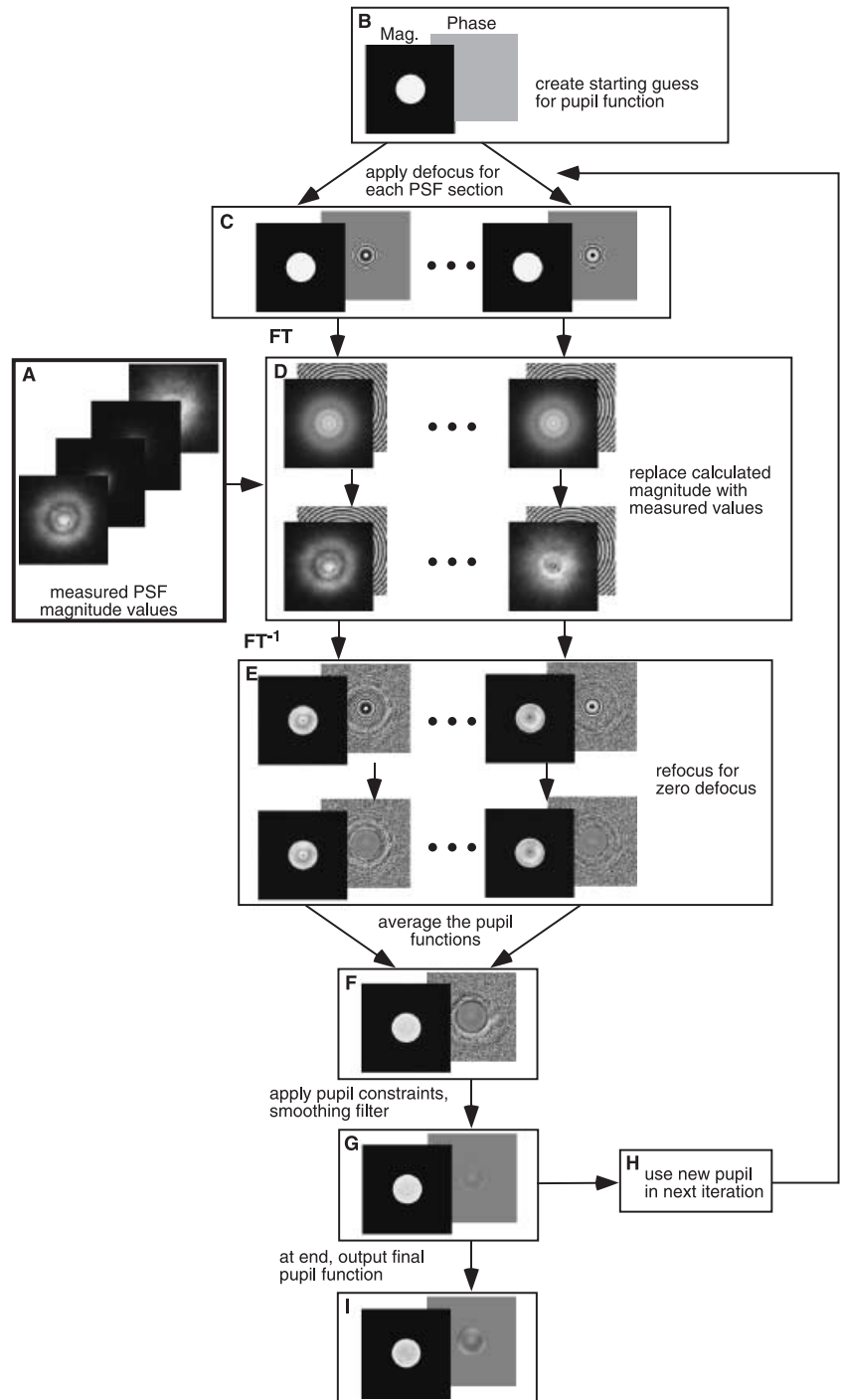


Fig. 2. Schematic of the phase retrieval algorithm. See text for details.

over the circular pupil defined by $k_x^2 + k_y^2 \leq (NA/\lambda)^2$. Equation (2) has the form of a 2D Fourier transform relationship between on the one hand the PSF section at a certain axial position z , and on the other hand the product $P(k_x, k_y)e^{2\pi i k_z(k_x, k_y)z}$. The factor $e^{2\pi i k_z(k_x, k_y)z}$ thus plays the role of a 'defocus phase function' that 're-focuses' the pupil function by a distance z . The above expression for the defocus phase function is exact for all apertures, because it merely expresses the spherical shape of OTF_A .

Phase retrieval

The phase retrieval method (Hanser *et al.*, 2003) is illustrated in Fig. 2. A series of defocus images (sections) of a subresolution point source, such as a fluorescent bead, were collected with different amounts of defocus and preprocessed as described above (Fig. 2A). A subset of these sections, usually four, were used in the phase retrieval. The phase retrieval process begins

with a starting guess of the pupil function (Fig. 2B); this is simply set to unity over the support defined by the objective lens NA and to zero elsewhere. The pupil function (which will in later iterations be complex-valued) is then multiplied by the phase function $e^{i2\pi k_z(k_x, k_y)z}$ that describes defocus by a distance z as explained in the previous paragraph. Setting z equal to the known axial position of each measured PSF section produces a defocus-adjusted pupil function that matches the axial position of that section (Fig. 2C). These defocus-adjusted pupils are two-dimensionally Fourier transformed to produce sections of the complex amplitude PSF corresponding to the starting pupil (Eq. 2). The magnitude values of these calculated PSF_A sections are then replaced by the square root of the corresponding sections of the measured intensity data, while their phase values are left unchanged (Fig. 2D). These magnitude-corrected PSF_A sections are Fourier transformed back to frequency space, and the defocus of each is readjusted back to zero by multiplying by the inverse defocus function $e^{-i2\pi k_z(k_x, k_y)z}$ (Fig. 2E). These four modified pupil functions (one for each of the four sections used) are averaged to produce a single pupil function estimate (Fig. 2F). The NA limit constraint is then imposed to remove spatial frequency values outside of the pupil limit. A smoothing filter may optionally be applied to the pupil function at this point to suppress noise (Fig. 2G); we used this filter at each iteration, but less frequent or no smoothing may be appropriate for low-noise data. This new pupil function estimate forms the starting pupil function for the next iteration (Fig. 2H). After a specified number of iterations or a stopping criterion has been reached, the final pupil function estimate is output (Fig. 2I). In this paper, we used a specified number of iterations – generally 25 iterations – and reported the intensity mean-square error (iMSE) for each iteration as a measure of phase retrieval quality.

We have also used the correlation coefficient (correl. coef.) as a supplementary, normalization-independent quality measure.

Corrections for bead size and vectorial effects

Two refinements to the imaging model of Hanser *et al.* (2003) were implemented, in order to take into account the finite size of the fluorescent bead and the vectorial nature of light. In this article we applied the corrections after the phase retrieval, but they could also be incorporated into the algorithm itself.

An intensity PSF measured using a finite-size bead as an approximate point source actually represents the true PSF convolved with the bead shape. Equivalently, the measured intensity OTF (the Fourier transform of the intensity PSF) is the true OTF multiplied by the Fourier transform $b(k)$ of the bead shape. If the fluorophore is uniformly distributed within a spherical bead, then $b(k) = 3h(\pi kd)$, where d is the bead diameter and $h(x) = \sin(x)/x^3 - \cos(x)/x^2$. For our parameters, $b(k)$ varies from 1 at the origin to 0.73 at the edge of the OTF support. To make phase-retrieved OTFs comparable with measured ones, they were multiplied by this function. An alternative strategy, not pursued here, would be to generate a ‘true’ PSF by dividing the measured OTF by $b(k)$, and retransforming to real space. This corrected PSF could then be used as the measured intensity PSF in the phase retrieval algorithm.

The vectorial nature of light was treated as follows (Fig. 3). We assumed that each volume element of the sample contains an ensemble of independently emitting fluorophore molecules, which we treated as uncorrelated dipole radiators with random orientations. At each instant, the molecular dipoles add up to a total dipole moment with uncorrelated x , y and z components. Thus we can model the ensemble as three mutually incoherent dipole radiators P_x , P_y and P_z of equal strength, orientated in the x , y and z directions, respectively. As the three dipoles are mutually incoherent, we can calculate the intensity image on the camera from each dipole separately, and add these images incoherently. Each dipole emits dipole radiation: the magnitude of the electric field E emitted in a certain ray direction is proportional to the sine of the angle β between the ray direction and the dipole vector, and the vector direction of E (i.e. the polarization) is given by the projection of the dipole vector onto the plane perpendicular to the ray direction (Jackson, 1999). To determine the effect of the objective lens on this field, we first decompose the electric field E of each ray into an azimuthal component E_ϕ and a ‘radial’ component with respect to the optic axis of the microscope. (The ‘radial’ component is actually orientated in the direction of increasing polar angle θ , as it must be perpendicular to the propagation direction.) By symmetry, these components must remain azimuthal and radial, respectively, after traversing the objective lens to reach the pupil plane. The ray appears in the pupil plane at a radial position r proportional to $\sin(\theta)$, as prescribed by the sine condition (Hecht, 1990, pp. 225–226). (They will

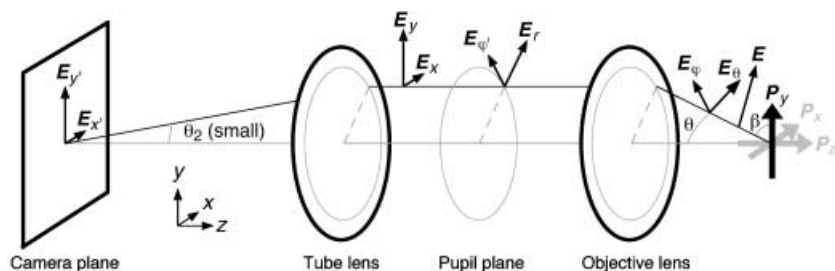


Fig. 3. The geometry for the vectorial PSF calculation. The trigonometric factors in Eq. (3) stem from coordinate transformations from spherical coordinates relative to the emitting dipole, to spherical coordinates relative to the optic axis, to cylindrical coordinates in the pupil plane, to Cartesian coordinates in the pupil and camera planes.

also both be rescaled by a factor $1/\sqrt{\cos(\theta)}$, where θ is the angle of the ray with respect to the optic axis, because of ‘wavefront compression’, i.e. energy conservation together with the fact that the relation between pupil plane area and emission solid angle depends on θ . This well-known factor can be ignored here as it is absorbed into our definition of the pupil function.) Once it has reached the pupil plane, the field is re-expressed in terms of its Cartesian components E_x and E_y , parallel to the x and y axis, respectively. These will remain x and y orientated after being formed into an image on the camera by the tube lens, because all ray angles are small in this part of the beam path. Being orthogonal, these x - and y -orientated field components will not interfere with each other, so their two intensity images can be calculated independently and added. Thus our calculation of the vectorially correct PSF simply consists of calculating and adding six intensity PSFs: each of the three x -, y - and z -orientated dipoles in the sample contributes one PSF for the x and one for the y polarization on the camera. In practice, each of these six component PSFs is calculated based on the pupil function (a single pupil function – it is assumed to be independent of polarization) exactly as is done in the usual phase retrieval method, except that for each component the pupil function is first multiplied by a particular real-valued trigonometric function resulting from the geometric considerations outlined above. These six functions are

$$\begin{aligned}
 P_x \rightarrow E_x: & \quad \cos(\theta) \cos^2(\varphi) + \sin^2(\varphi) \\
 P_x \rightarrow E_y: & \quad (\cos(\theta) - 1) \sin(\varphi) \cos(\varphi) \\
 P_y \rightarrow E_x: & \quad (\cos(\theta) - 1) \sin(\varphi) \cos(\varphi) \\
 P_y \rightarrow E_y: & \quad \cos(\theta) \sin^2(\varphi) + \cos^2(\varphi) \\
 P_z \rightarrow E_x: & \quad \sin(\theta) \cos(\varphi) \\
 P_z \rightarrow E_y: & \quad \sin(\theta) \sin(\varphi)
 \end{aligned} \tag{3}$$

These are the same trigonometric functions as appear in the classic calculation by Richards & Wolf (1959) of focused vectorial light fields – the two approaches are in fact equivalent.

As described in the Results section, we found that high-spatial-frequency components are systematically over-emphasized in phase-retrieved PSFs compared with the original measured data. Inclusion of bead size and vectorial effects in the PSF calculation only partially account for this observed difference. Therefore, we introduced an empirical rescaling function to attenuate the high-spatial-frequency components. We divided the intensity OTF of a typical measured PSF data set by the OTF produced by phase retrieval of the same data set, and least-squares-fitted a function of spatial frequency to this ratio. This function was then used to rescale other phase-retrieved PSFs: the PSF in question was Fourier transformed (to form the OTF), multiplied by the empirical rescaling function, and re-transforming to real space. We

selected the OTF rescaling function to be a Gaussian, as this form roughly matched the observed curve shape. Owing to low signal-to-noise levels in the highest-frequency regions of the measured OTF, which was collected with an NA = 1.3 objective, we performed the fit on a subset of the OTF corresponding to the smaller OTF support of an NA = 1.15 objective.

Zernike expansion of pupil functions

Pupil functions were sometimes expanded in a basis of orthogonal functions, to make the description even more compact, to simplify evaluation of the system in terms of classical aberrations, and to suppress noise. The basis chosen was the Zernike polynomials. We used a set of 79 basis functions, consisting of all the Zernike polynomials up through radial order 11, plus the purely radial polynomial of order 12. The magnitude and phase components of the pupil functions were fitted separately to the polynomials using a linear least-squares fitting routine. Prior to fitting the phase component, the phase was unwrapped using a simple linear extrapolation method.

Phase retrieval from measured, aberrated PSFs

Bead images containing aberrations caused by an oil drop in glycerol were collected as described in Kam *et al.* (2001). These PSFs were processed as described above, except that six defocus sections spaced 1.25 μm apart were selected and used in the phase retrieval.

Calculation of the aberration function for refractive index mismatch

Consider a point source located at a depth d below the cover slip, in a mounting medium of index n_2 , observed with an objective lens designed for an immersion medium with a refractive index n_1 (Fig. 4). We want to calculate the aberration function, i.e. the change, caused by the mismatch of n_2 and n_1 , in the complex amplitude (phase and magnitude) of each light ray from this source, as a function of the position at which that ray crosses the back focal plane pupil of the objective lens. A given position in the pupil corresponds to a given angle θ_1 of the ray in the immersion medium, so we want to compare aberrated and unaberrated rays with the same θ_1 . The phase change is determined by the difference between the optical path length travelled to the pupil by a ray that leaves the source at an angle θ_2 relative to the optic axis and is refracted to the angle θ_1 upon leaving the mounting medium, and the optical path length that a ray with angle θ_1 would have travelled if the mounting medium index were the ideal index n_1 . With simple geometry one can show that this path length difference is

$$OP(\theta_1, \theta_2, d, n_1, n_2) = d(n_2 \cos(\theta_2) - n_1 \cos(\theta_1)). \tag{4}$$

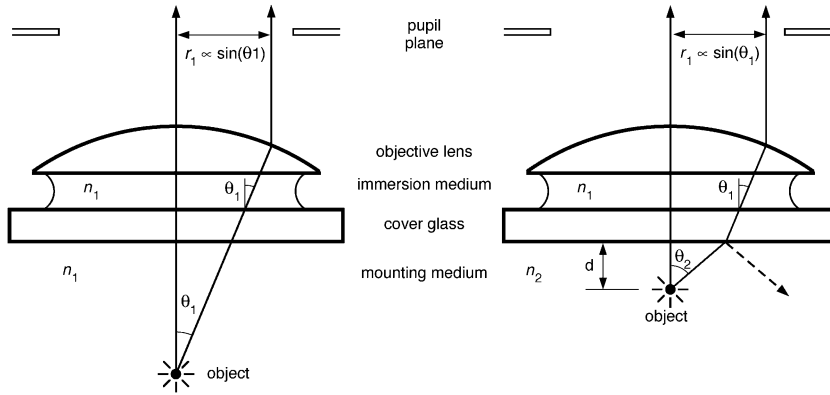


Fig. 4. The geometry for calculating depth-dependent index-mismatch aberrations. The paths of rays that end up at a given radius r_1 in the pupil plane, for (left) the ideal case when the refractive index of the mounting medium equals that of the correct immersion medium for the objectives, and (right) the case when the mounting medium index is mismatched. In the latter case the phase and magnitude of the wave front in the pupil plane will be distorted by the aberration function calculated in Eqs (4)–(8).

θ_2 and θ_1 are of course related to n_1 and n_2 by Snell's law, $n_1 \sin \theta_1 = n_2 \sin \theta_2$.

There are also angle-dependent magnitude changes, caused by two effects: reflection losses and wavefront compression. The losses due to Fresnel reflection at the n_1/n_2 interface are polarization-dependent, but in this calculation we ignore polarization and set the overall transmittance to the average of the polarized transmittance factors (Hecht, 1990, pp. 94–102):

$$A_t(\theta_1, \theta_2, n_1, n_2) = [\sin \theta_1 \cos \theta_2 / \sin(\theta_1 + \theta_2)][1 + 1/\cos(\theta_2 - \theta_1)]. \quad (5)$$

What we call wavefront compression results from the fact that the refraction of rays at the n_1/n_2 interface causes each area element in the pupil plane to receive light from a different amount of emission solid angle around the bead than it otherwise would have, so the wavefront magnitude must be rescaled to satisfy conservation of energy. This factor can be shown to be

$$A_w(\theta_1, \theta_2, n_1, n_2) = n_1 \tan \theta_2 / n_2 \tan \theta_1. \quad (6)$$

Equations (4)–(6) can be converted from the angular coordinates θ_1 and θ_2 to k_x and k_y , the Cartesian spatial frequency positions on the pupil plane, as θ_2 is determined by θ_1 through Snell's law, and θ_1 relates directly to k_x and k_y according to the sine condition:

$$\sin \theta_1 = \frac{\lambda}{n_1} \sqrt{k_x^2 + k_y^2}. \quad (7)$$

The total aberration function is:

$$\Psi(k_x, k_y, d, n_1, n_2) = A(k_x, k_y, n_1, n_2) e^{i2\pi OP(k_x, k_y, d, n_1, n_2)/\lambda}. \quad (8)$$

where $A = A_t A_w$. If this function is multiplied with an unaberrated pupil function $P(k_x, k_y)$ of a particular microscope, the result is a combined pupil function

$$P'(k_x, k_y, d, n_1, n_2) = P(k_x, k_y) \Psi(k_x, k_y, d, n_1, n_2) / \lambda \quad (9)$$

that describes how that microscope would perform under the index-mismatched conditions. This modified pupil function

can be used as previously described to produce an intensity PSF that contains the aberration.

Image deconvolution

To generate a well-defined test object for deconvolution tests, a simulated dataset containing a number of objects was convolved with a measured PSF, producing a blurred simulated test dataset. To minimize aliasing effects from the discrete, FFT-based convolution, only a subregion of the blurred test dataset was used as the input dataset for the deconvolution tests.

As described below, this input dataset was then deconvolved by the various measured and calculated PSFs using 50 iterations of Gold's (ratio) method (Agard *et al.*, 1989), modified to use PSFs that are not rotationally symmetric. The quality of the deconvolution was judged subjectively by comparing the deconvolution result (the estimated object) to the original object, and quantitatively by re-blurring the estimated object through convolution with the relevant PSF (so that the result would ideally reproduce the input image data), and then calculating the R -factor:

$$R = \frac{\overline{|f(x) - g(x)|}}{\overline{|f(x)|}}, \quad (10)$$

which represents the pixel-wise difference between the blurred, estimated object $g(x)$ and the input image $f(x)$, averaged over all pixels in the data set and normalized by the average intensity of the input image pixels.

Results

Evaluation and of phase-retrieved intensity PSF and OTF

The phase retrieval algorithm typically converged toward a stable pupil function in a few tens of iterations. Figure 5(A,B) show the magnitude and phase components, respectively, of a pupil function produced by phase retrieval from a measured PSF data set acquired under ideal conditions. As can be seen, the phase-retrieved pupil functions contain strong and strikingly

asymmetric phase deviations, indicating that the optical wavefront is significantly distorted from its optimal spherical shape. In an ideal pupil function the phase would be constant and the magnitude would vary smoothly with radius as $1/\sqrt{\cos(\theta)}$ – this non-constant magnitude distribution is a result of the ‘wavefront compression’ factor mentioned in the methods. The magnitude component in Fig. 5(A) shows that, for this particular microscope system, the pupil function magnitude deviates from the theoretical ideal throughout the pupil, and these deviations are not rotationally symmetric. The phase component (Fig. 5B) deviates even more strongly from the ideal. The autocorrelation of the pupil function is the intensity OTF; the magnitude and phase of an axial section of this is shown in Fig. 5(C,D). The aberrations observed in the phase-retrieved pupil function are reflected as phase variations within the intensity OTF (Fig. 5D).

Figure 6 shows an intensity PSF that was reconstructed from a phase-retrieved pupil function (middle row), compared with the original, measured PSF used in the phase retrieval (top row). Most features of the measured data are quite well reproduced by the phase-retrieved PSF, both in individual lateral sections (Fig. 6, left three columns) and in axial views (Fig. 6, right column).

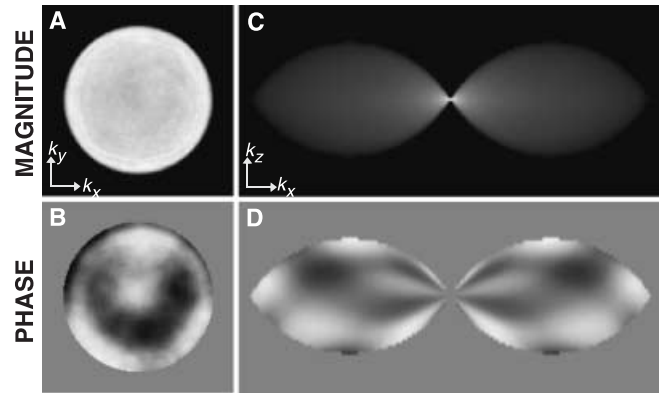


Fig. 5. Phase retrieval results. The magnitude (A, shown with a greyscale ranging from the minimum to maximum value) and phase (B, scale $\pm \pi/4$) components of the pupil function. The magnitude (C, scale from minimum to maximum with a gamma (greyscale non-linearity) of 0.5) and phase (D, scale $\pm \pi/4$) components of the intensity OTF calculated from the pupil function.

Under careful scrutiny, one subtle but systematic difference does appear: many structures appear slightly sharper in PSFs reconstructed from pupil functions than they do in the corresponding measured PSFs. This is particularly apparent in the

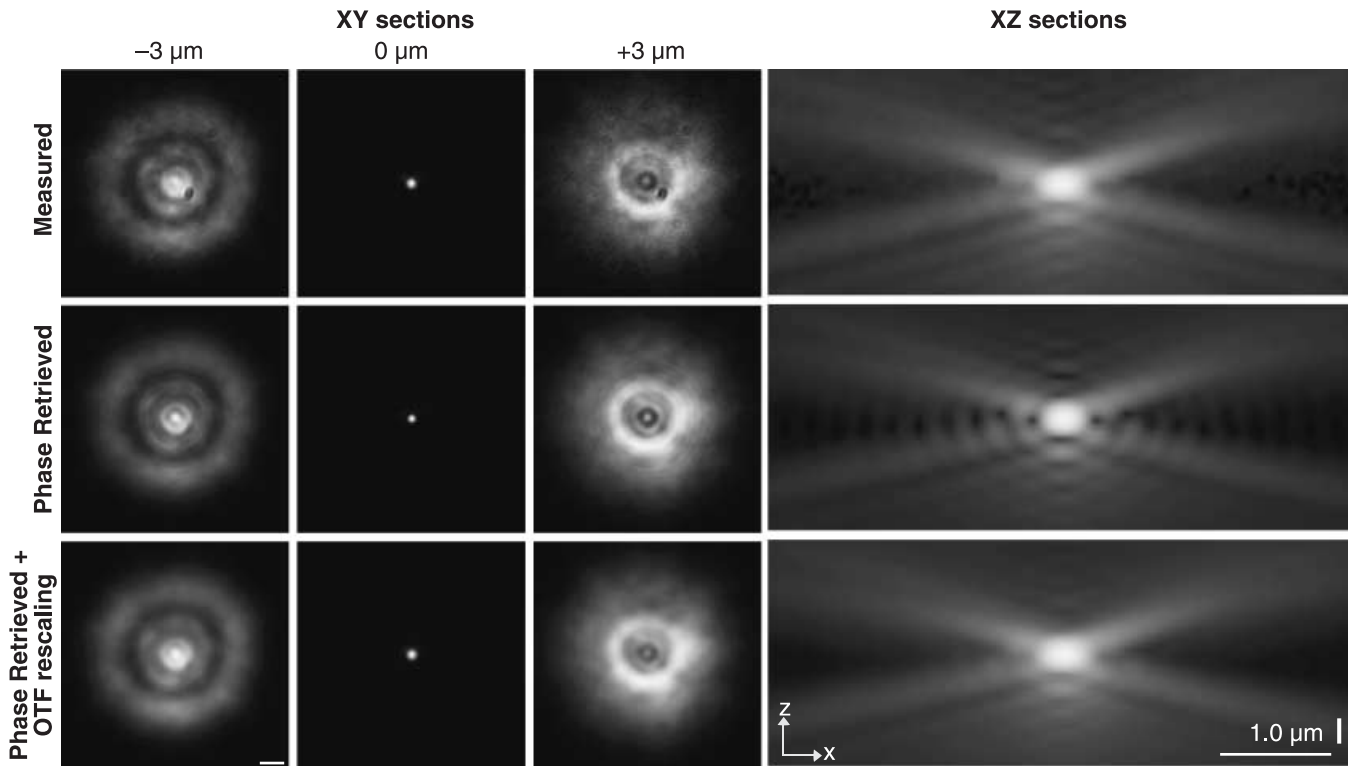


Fig. 6. Comparison of measured and phase-retrieved PSFs. Top row: three lateral sections and one axial section through a measured PSF. Middle row: equivalent sections of a PSF calculated from the phase-retrieved pupil function for the same measured PSF. The features observed in the measured data are reproduced well, but high spatial frequencies are slightly over-emphasized. Bottom row: the phase-retrieved PSF after application of the OTF rescaling, improving the match to the measured data. The axial sections are displayed with a non-linear greyscale to enhance the weak out-of-focus features. All scale bars = 1.0 μm .

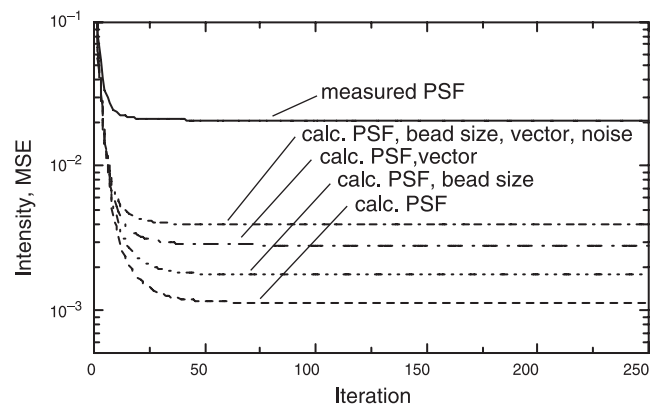


Fig. 7. Intensity mean square error (iMSE) values plotted vs. iteration number during the phase retrieval, illustrating convergence of the algorithm. The starting data for phase retrieval were a measured PSF dataset acquired under ideal conditions (top, solid line) and four PSF datasets that were themselves constructed from pupil functions, modified as follows (bottom to top): not modified; modified to take into account the bead size; modified to use a vectorially correct imaging model; and modified to include both bead size and vectorial effects as well as noise. The level of residual error seen with the measured data is partly but not fully explained by these effects.

axial views (Fig. 6, right column). We have studied this phenomenon through its effects on the fitting error during phase retrieval and on the power distribution in frequency space, as will be discussed in the next two paragraphs, which also describe an *ad hoc* method to compensate for the effect.

To assess the extent to which phase-retrieved pupil functions can accurately reproduce measured intensity PSF data, we evaluated the results both during and at the end of the iterative phase retrieval process. As a figure of merit for the phase retrieval, we used the iMSE between the original measured intensity PSF data and the intensity PSF that was reconstructed from the pupil function. As illustrated in the top, solid, trace in Fig. 7, the iMSE value initially dropped rapidly, but then stabilized at a non-zero residual error value. That the iMSE did not converge to zero raises the question of whether the reason lies (i) in poor convergence of the algorithm or (ii) in the imaging model being imperfect so that no pupil function could describe the data exactly. To distinguish between these two possibilities, we reconstructed a PSF data set from a pupil function using the same imaging model, so that we knew by construction that it could indeed be described by a pupil function, and repeated the phase retrieval on this simulated data set. The result was much lower error values (Fig. 7, bottom trace). This suggests that hypothesis (ii) was the case: that the fault for the residual errors lay not with the phase retrieval algorithm, but in that the simple imaging model used up to that point was insufficient for describing the measurement. That model had two known deficiencies: it ignored the vector nature of light and the finite size of the bead used as a ‘point source’ to acquire the PSF data. Another known source of

residual error was the measurement noise in the measured PSF data. To investigate whether these known effects could explain the residual error, we constructed further simulated PSFs from the same pupil function as before, but included some or all of the above effects in the calculation (as explained in the Methods). Phase retrievals on these data sets did produce higher error values, as expected (Fig. 7, centre three traces), but not as high as the measured PSF. The unaccounted-for residual error would seem to indicate that the imaging model is still imperfect even after bead size, vectorial effects and noise have been taken into account. A similar phenomenon was also observed in frequency space, as described in the next paragraph.

In order for the phase-retrieved pupil function to serve as a replacement for a measured intensity PSF, the intensity PSF calculated from the pupil function must match the measured data in frequency space as well as in real space. To evaluate the frequency space properties, we compared the intensity OTFs for measured and corresponding phase-retrieved PSFs. Figure 8 shows line profiles across the intensity OTF, along the k_x axis

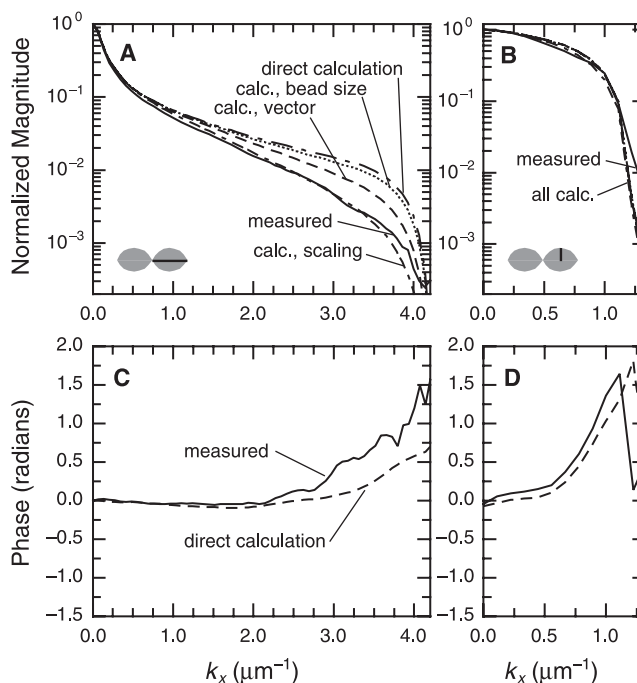


Fig. 8. Comparison of line profiles through intensity OTFs corresponding to some of the PSFs used in Fig. 5(A). Normalized magnitude (A,B) and phase (C,D) profiles along (A,C) the k_x axis as indicated by the black line in the OTF cartoon in the bottom left corner of A, and (B,D) in the k_y direction at $k_x = 2.14 \mu\text{m}^{-1}$ as indicated by the cartoon in B. The calculated traces in B are similar to each other and partly overlap in the figure. In C and D, phase traces for the modified calculated OTFs are not shown as they do not differ significantly from the directly calculated one. Note that OTFs calculated from pupil functions fall off less rapidly with lateral frequency than measured OTFs, and that this is only partially explained by bead size and vectorial effects; this observation motivated the introduction of the OTF rescaling function. The trace marked ‘scaling’ (in A, B) includes the rescaling function but is an otherwise unmodified calculation.

(Fig. 8A,C) and along a k_x line at the widest k_x position (Fig. 8B,D). The major difference observed is that the magnitude of the intensity OTF decreases more rapidly as a function of spatial frequency for the measured data (solid line in Fig. 8A,B) than for the phase-retrieved PSF. This effect can be partially explained by taking into account vectorial effects. Compensating for the finite size of the bead used to acquire the measured PSF only produces a small change, and these corrections together were not sufficient to explain the difference (Fig. 8A). We therefore decided to introduce an empirical rescaling function, explicitly to make the phase-retrieved intensity OTF match the more rapid falloff of intensity with frequency that is seen in the measured OTFs. A Gaussian function was fitted to the point-wise ratio of a typical measured OTF to its corresponding phase-retrieved OTF, and was used to rescale the magnitude of this and other phase-retrieved OTFs, as described in the Methods. With this rescaling function in place, it was not necessary to include the vectorial and bead size corrections in the phase retrieval procedure, as the main effect of these consists of faster OTF falloff and is thus absorbed into the OTF rescaling function. Some phase deviations between the measured and phase-retrieved OTFs can also be observed (Fig. 8C,D), but these are not consistent from dataset to dataset and occur mainly in the low-signal-to-noise regions at the edge of the OTF.

When this OTF rescaling function is applied to the PSF reconstruction shown in the middle row of Fig. 6, it eliminates the excess sharpness (Fig. 6, bottom row) and improves the match quantitatively: the iMSE for the sections shown decreases from 0.0169 (and a correl. coef. of 0.9915) for the PSF directly reconstructed from the pupil function to 0.0102 (correl. coef. 0.9948) after the rescaling is applied. The error improvement is even more significant for the in-focus section (data not shown), where the iMSE improves by a factor of 4 to 0.0197 (the correl. coef. changes from 0.9559 to 0.9901). The final PSF thus reproduces the microscope-specific features of the measured PSF at a realistic level of sharpness.

An interesting observation is that the dark spot near the centre of the measured PSF in Fig. 6 (top), which is due to a dust particle on a window close to the CCD camera, is nearly absent in the phase-retrieved PSFs (middle and bottom rows). The same is true for several ring-like features, also caused by dust. As the dust-related image structures do not change with defocus in the way that would be expected for actual PSF features, they cannot be described by a pupil function, and are therefore suppressed during the phase retrieval process. This removal of artefacts is a positive side-effect from elimination of redundancy when a 3D PSF is reduced to a 2D pupil function.

Expanding pupil functions in Zernike polynomials

In some situations it may be desirable to expand the pupil function in a set of basis functions, so as to reduce further the description of the optical system to a small number of coefficients. Such a compact, parameterized description lends itself

well, for instance, to manipulation and fitting, as in semi-blind deconvolution approaches. The inherent filtering involved in any truncated expansion also reduces the fine-scale noise in the pupil function that results from the measurement noise in any individual measured starting PSF. One attractive choice of basis is the Zernike polynomials, which are widely used in the analysis of aberrations in optical systems (Noll, 1976; Mahajan, 1994). This basis has the advantage that each coefficient is associated with a specific classical aberration, so that the coefficient values from a Zernike polynomial fit can provide direct information about the aberrations present in the optical system.

Figure 9 shows a pupil function fitted to a set of 79 Zernike polynomials. The resulting fit (centre column) retains the large-scale features while removing the smaller-scale features, as can be seen in the residual difference (right – shown with expanded greyscale) between the original pupil function (left) and its Zernike fit. When the PSF reconstructed from the Zernike-fitted pupil function was compared with the original, measured PSF, the error (iMSE) was 0.0107 and the correl. coef. was 0.9946. These values are nearly identical to the iMSE of 0.0102 (and correl. coef. of 0.9948) that resulted when using the un-fitted pupil function. The OTF rescaling was used in both cases. The Zernike-fitted pupil function thus fits the starting data almost exactly as well as the un-fitted pupil function does. The error was expected to rise slightly upon Zernike-fitting, because the original pupil function produced by phase retrieval should by construction be optimal for the measured PSF starting data, including its particular noise and background error. Part of the small error increase observed may in fact represent a desired elimination of unwanted noise-related features from the pupil function.

Phase retrieval in the presence of a phase ring

To demonstrate the ability of phase retrieval to reproduce features in the pupil, we introduced a known magnitude and phase deviation into a pupil plane of the microscope optical path in the form of a phase ring. On the Zeiss Axiomat, a phase plate may be inserted into the optical path, in combination with an annular aperture in the illumination path, for phase contrast imaging. The phase plate consists of a ring with a nominal $\pi/2$ phase difference relative to the rest of the plate. The phase shift is typically calibrated for green light; for $\lambda \sim 520$ nm, a $\pi/2$ phase shift corresponds to 130 nm of optical path change. Phase rings generally also attenuate the light passing through the ring, to improve contrast. Because the phase ring is located in a plane that is conjugate to the primary pupil plane, the phase and magnitude features of the phase ring would be expected to cause directly corresponding features in the pupil function.

With a phase ring in the optical path, a PSF was collected (using stepped exposure time) and used in 25 iterations of phase retrieval. The final iMSE was 0.0402. Figure 10(A,B) show the magnitude and phase components, respectively, of

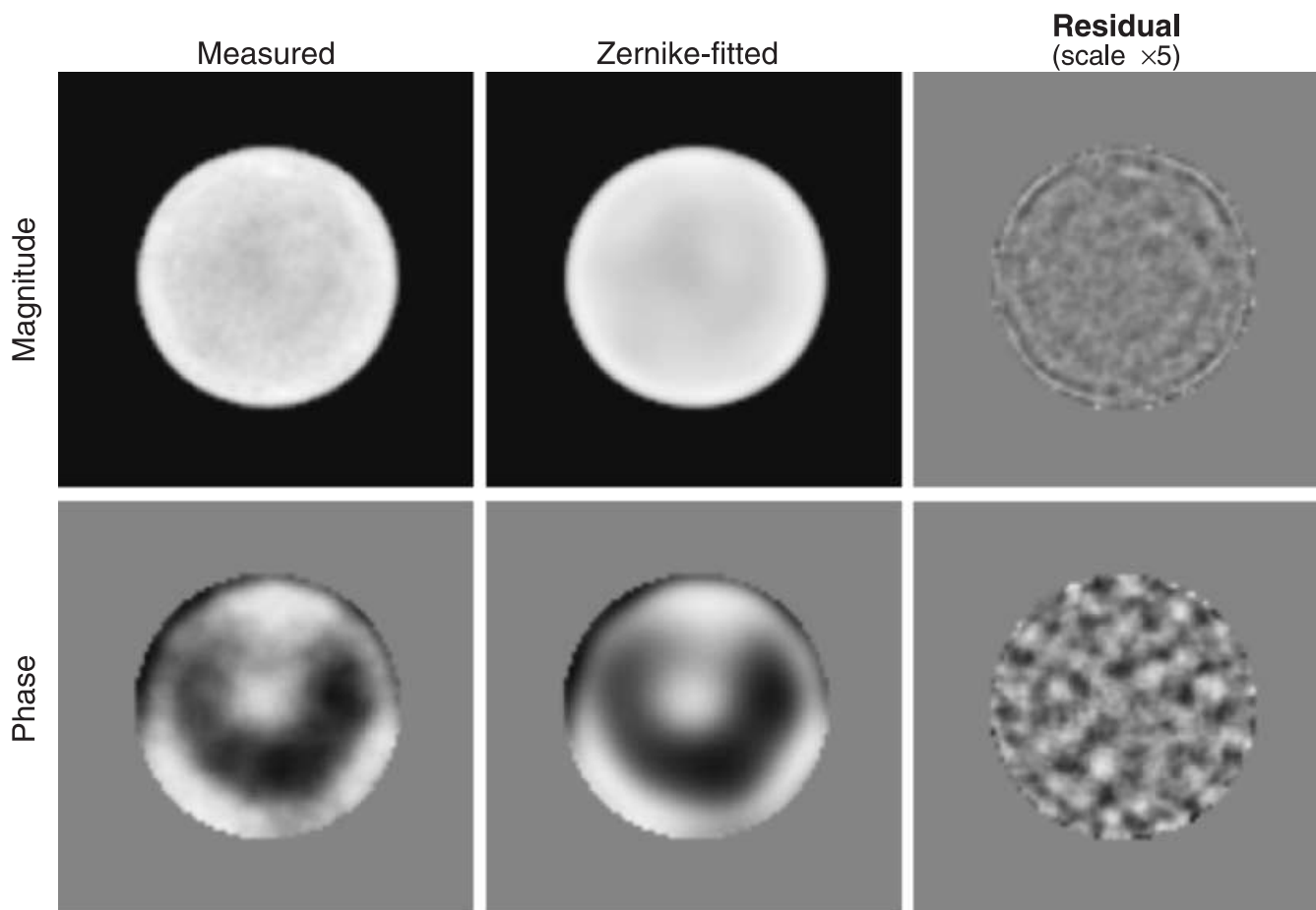


Fig. 9. Fitting of a phase-retrieved pupil function to a basis of Zernike polynomials. The magnitude (top) and phase (bottom) components are shown for the original phase-retrieved (left) and Zernike-fitted (centre) pupil function, with the residual difference between the two pupil functions shown, rescaled, on the right. The greyscale ranges from 0 to the maximum value of the original phase-retrieved pupil for the phase-retrieved and Zernike-fitted pupil functions, ± 0.2 of the maximum phase-retrieved magnitude value for magnitude residual, $\pm \pi/4$ for the phase component of the two pupil functions, and $\pm \pi/20$ for the phase residual.

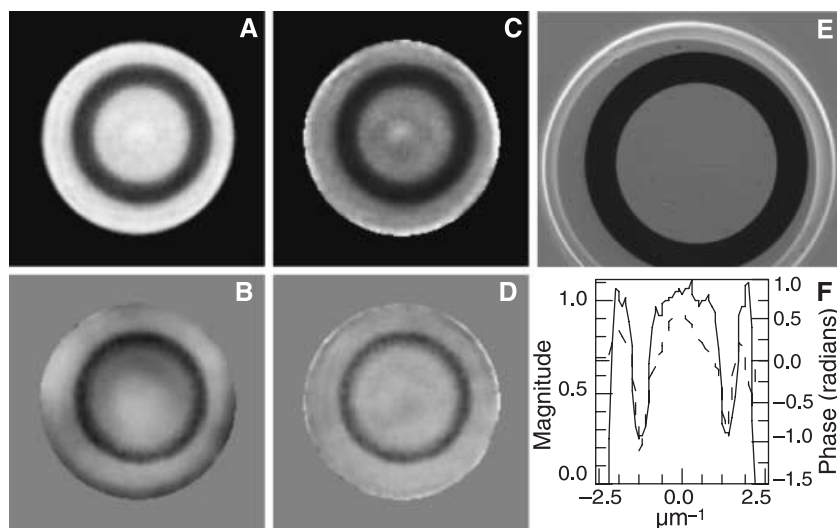


Fig. 10. Ability of a phase-retrieved pupil function to describe pupil-plane features. (A,B) Magnitude and phase components, respectively, of a pupil function phase-retrieved from a measured PSF acquired with a phase ring in the optical path. (C,D) The pupil function in A and B divided by a phase-retrieved pupil function representing the same optical path without the phase ring in place. (E) A directly measured image of the phase ring itself, collected using a Bertrand lens. (F) Line profile data through the centre of the pupil function shown in A and B, showing that the magnitude and phase features associated with the phase ring overlap spatially.

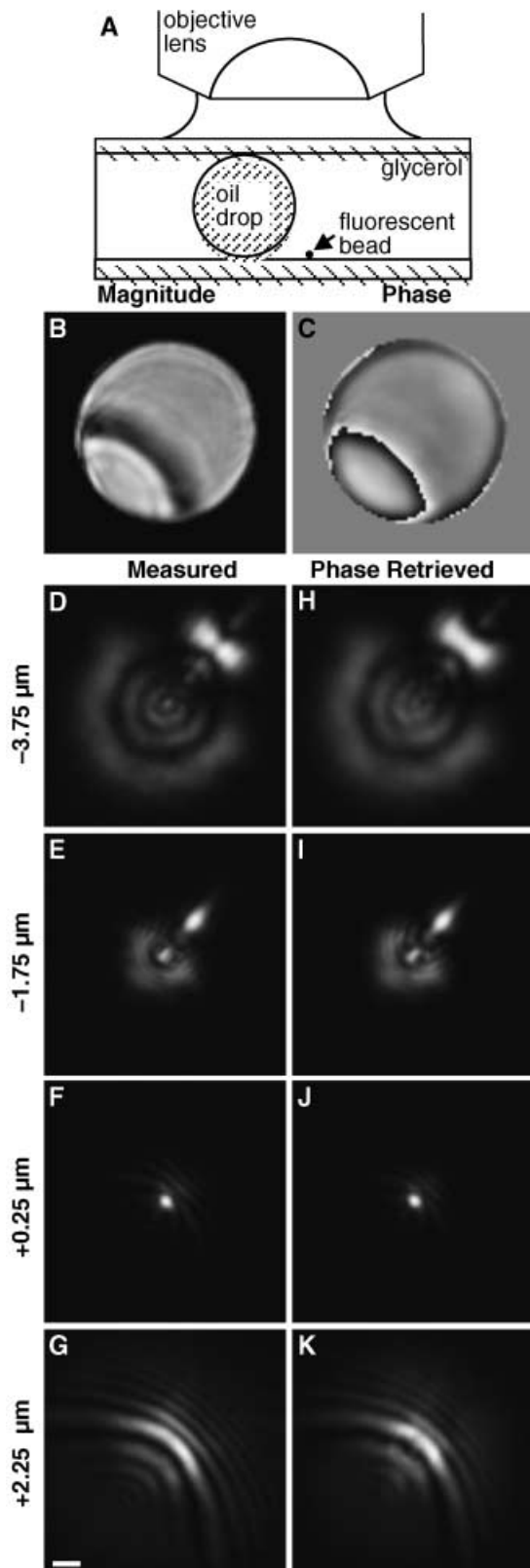


Fig. 11. Ability of a phase-retrieved pupil function to describe sample-induced aberration. A fluorescent bead was mounted in glycerol with an oil drop in the optical path (A). The magnitude (B) and phase (C)

the resulting pupil function. The ring feature is obvious in both components. In Fig. 10(C,D), the pupil function with the phase ring has been divided by a pupil function without a phase ring, to show the ring more clearly by minimizing the effect of phase-ring-independent features of the optical path. The ring shape is well defined and uniform, though not perfectly sharp, especially in the phase component. The magnitude attenuation of the ring feature in the phase-retrieved pupil function was measured to 0.37, and the maximum phase deviation was about 65° at $\lambda = 615$ nm, corresponding to 111 nm of optical path change. To allow a comparison, the actual magnitude attenuation of the phase ring was directly measured by imaging the back focal plane of the microscope with the aid of a Bertrand lens inserted into the optical path (Fig. 10E). After correcting for background levels and magnitude deviations not related to the inserted phase ring, we measured a magnitude attenuation of 0.39 on the Bertrand lens image, in close agreement with the 0.37 result of the phase retrieval. Additionally, magnitude and phase line profiles through the centre of the pupil function in A and B show that the magnitude and phase ring features overlap spatially, as would be expected (Fig. 10F).

Phase retrieval in the presence of severe sample-induced aberrations

Many biological samples contain strong variations in refractive index, which cause severe aberrations in the images observed through a microscope. Unlike the phase ring case considered above, where the disturbance is located in the pupil plane at infinite distance from the sample, the sample-induced aberrations originate very close to the source. To demonstrate in a controlled manner that phase retrieval can describe this type of aberration accurately, we used a simple model of sample-induced aberrations: a fluorescent bead was immersed in glycerol and a large, spherical oil drop was located between the bead and the cover slip (Fig. 11A). A PSF dataset was collected on this sample using a constant exposure time, and a pupil function calculated from that data set using phase retrieval (Fig. 11B,C). Large deviations in both magnitude and phase can be seen in the pupil function, representing the aberrating effects of the oil drop in the optical path. These deviations are similar to those observed on the same object by an alternative, ray-tracing method (Kam *et al.*, 2001; data not shown). In Fig. 11(D–K), the PSF calculated from this pupil function is compared with the original, measured PSF. The large oil drop near the bead causes the PSF to be severely asymmetric with curved ripples on one side of focus and out-of-focus rings with a high-intensity flare pointing away from the oil drop on the

components of the phase-retrieved pupil function show the significant aberrations caused by the oil drop. The PSF generated from the phase-retrieved pupil function (H–K) reproduces the features seen in the measured PSF (D–G). Scale bar = 1.0 μ m.

other side of focus (Fig. 11D–G). The phase-retrieved PSF reproduces these features well (Fig. 11H–K), with an iMSE of 0.0323 (correl. coef. 0.9840) after OTF rescaling.

Modification of pupil functions by calculated aberration functions

An important feature of pupil functions is that they can easily be modified to include any known aberration, simply by multiplying the pupil function by an aberration function (Eq. 9). In this section we demonstrate this process on the particular case of index-mismatch aberrations. These mainly spherical aberrations, which increase in severity with imaging depth, are encountered whenever the sample has a different refractive index than the objective lens was designed for. The aberration function for this situation is straightforward to calculate theoretically (Eqs 4–8). We wanted to demonstrate that the behaviour of a particular microscope in the presence of these aberrations can be well described by modifying an un-aberrated phase-retrieved pupil function with a calculated aberration function. For this purpose, we measured a series of PSFs on beads located at increasing depths under water, using the support ball device described in the Methods. The PSF measured at zero depth was used to calculate an ‘un-

aberrated’ pupil function. For each remaining measured PSF, we calculated the aberration function for that depth, multiplied it with the un-aberrated phase-retrieved pupil function to produce an aberrated pupil function, and used that to calculate the corresponding PSF. These calculated PSFs were compared with the measured PSFs (Fig. 12). The major features of PSFs calculated from the modified phase-retrieved pupil functions (centre column) match quite well with the measured data (left column). The equivalent purely theoretical PSFs (right column) match the general axial asymmetry of the measured PSFs, but contain noticeable differences. In particular, the central higher intensity region on the more blurred side of focus is more localized and peaked in the theoretical PSF, whereas the measured and phase-retrieved PSFs show a broader distribution of higher intensity values within a residual defocus ring. The PSFs produced from the modified phase-retrieved pupil functions are far more similar to the measured data in this regard. Thus a single phase-retrieved pupil function suffices to describe the imaging properties of a particular microscope at any desired depth. To produce a PSF for a given depth, one need only multiply the phase-retrieved pupil function by the corresponding calculated aberration function for that depth.

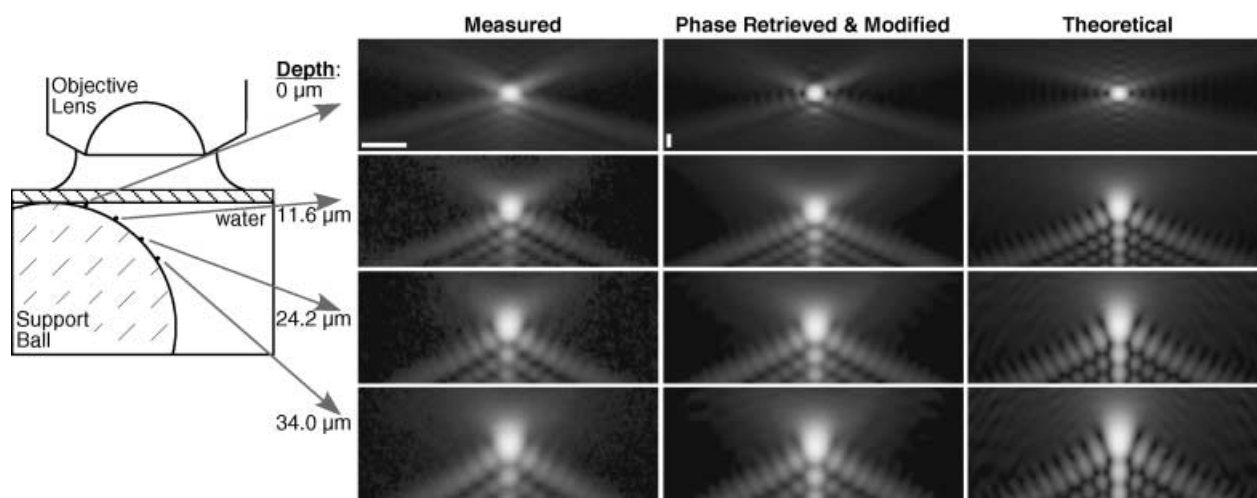
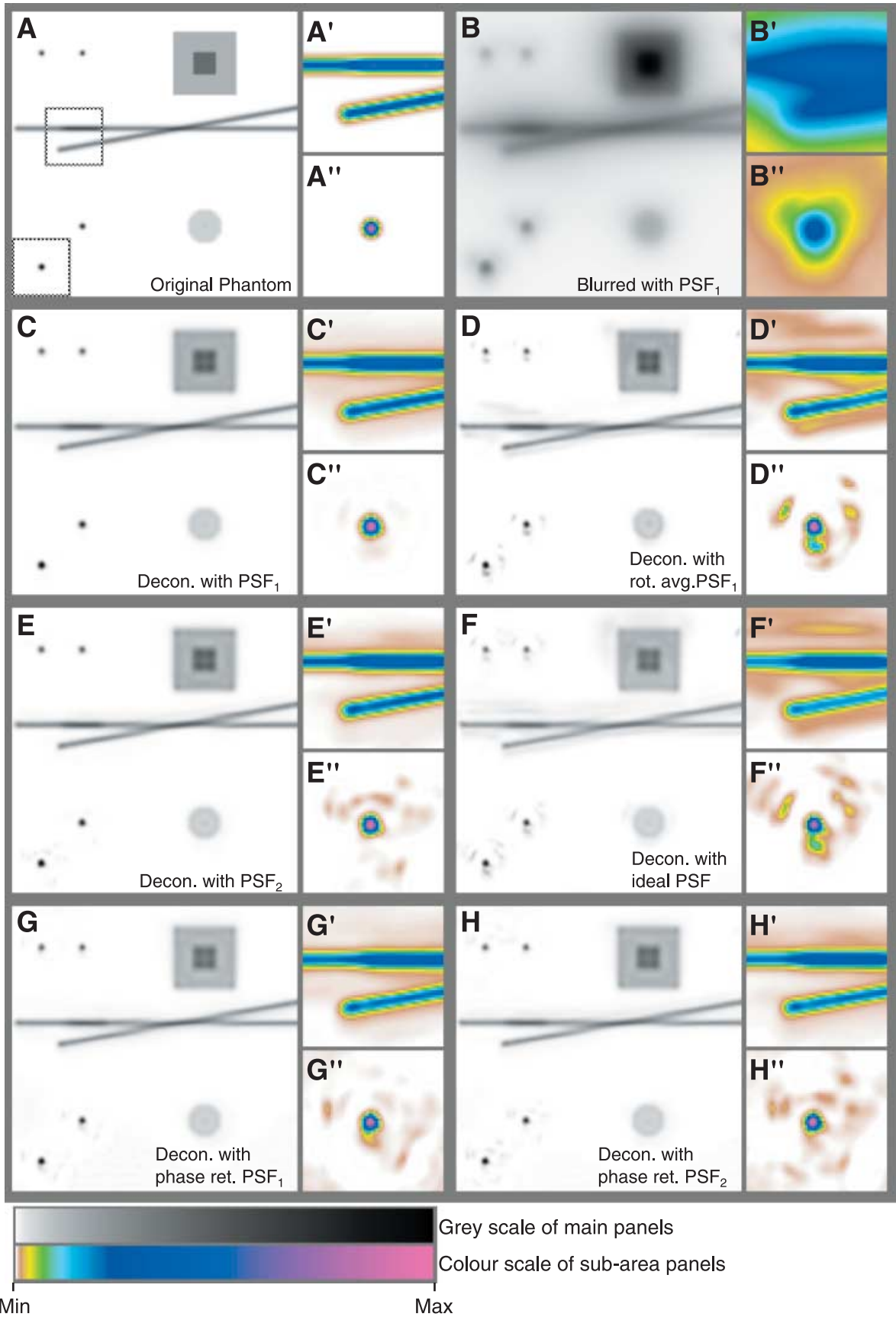


Fig. 12. Modification of a phase-retrieved pupil function using calculated aberration functions. To produce index-mismatch aberrations, fluorescent beads were mounted under various depth of water (schematic at left), and imaged with an oil-immersion objective lens. Axial sections of the measured PSFs are shown in the left column of images. Corresponding calculated depth aberrations were applied to a phase-retrieved pupil function containing no depth aberration, and PSFs were calculated (centre column). The right column shows purely theoretical PSFs for the same depth aberrations; these lack microscope-specific features. Scale bars = 1.0 μm .

Fig. 13. Deconvolution using phase-retrieved PSFs. Average-intensity projections over a 1.75- μm range are shown for (A) the original simulated dataset, (B) the simulated dataset blurred by a measured PSF, PSF_1 , and (C–H) results from deconvolution of the blurred dataset. The PSFs used in the deconvolution are as follows: (C) PSF_1 ; (D) a rotationally averaged version of PSF_1 ; (E) PSF_2 – a different measured PSF for the same optical system as PSF_1 ; (F) a theoretical, ideal PSF; (G,H) PSFs calculated from a phase-retrieved pupil function for PSF_1 and PSF_2 , respectively, using the OTF rescaling. The images are shown with a non-linear, inverted (i.e. darker = higher intensity) greyscale to emphasize weak features. To make it easier to compare the faint deconvolution artefacts, two subsets of each image, corresponding to the boxes marked in A, are shown with a colour scale to the right of each main panel.



Deconvolution using phase-retrieved PSFs

Deconvolution processing of 3D microscopy images is one field that requires an accurate PSF, and is a major potential application for phase-retrieved pupil functions. Therefore, it is important to establish whether PSFs calculated from a phase-retrieved pupil function are usable for deconvolution. In order to test this, a test data set (Fig. 13B) was generated by constructing a phantom object dataset (Fig. 13A) and computationally blurring it by convolution with a measured PSF dataset (which we will call PSF_1). The original phantom object dataset contained three crossed rods, a number of point-like objects of varying intensity, a sphere and a cube set into a larger cube with lower intensity. The point-like and 3D objects have their centres in the central axial plane of the dataset, and two of the rods also lie in this plane. The third rod is orientated obliquely to this plane; the region where it crosses one of the other rods at an angle appears in Fig. 13(A) as a denser region on that rod. The blurred test dataset was deconvolved for 50 iterations by either measured (Fig. 13C,E), theoretical (Fig. 13F) or phase-retrieved (Fig. 13G,H) PSFs. Two different measured PSFs were used: the original dataset PSF_1 and another PSF, dataset PSF_2 , acquired on the same microscope. PSF_1 and PSF_2 are very similar because they represent the same optical system, but they contain different measurement noise. Figure 13 shows average intensity projections for the central seven sections of the datasets, spanning a depth range of $1.75\ \mu\text{m}$.

The deconvolution results shown in Fig. 13 show that the visually best result, as would be expected, comes from using PSF_1 (Fig. 13C), the same PSF that was used to blur the test dataset. That deconvolution produced a final R -factor (defined in Eq. 10) of 0.1159. Using the independent but nominally identical measured PSF, PSF_2 , produced a slightly higher R -factor of 0.1289 as would be expected owing to the independent noise. Very slight artefacts can also be discerned around the point-like objects (Fig. 13E,E''), which indicates that the aberrations of the microscope are not perfectly reproducible from data set to data set. PSFs generated from phase-retrieved pupil functions corresponding to PSF_1 (Fig. 13G) and PSF_2 (Fig. 13H) yielded results similar to that of PSF_2 , and their R -factors (0.0942 and 0.1042, respectively) were actually slightly better than those of either measured PSF. There are some faint artefacts in the deconvolutions using the phase-retrieved PSFs (Fig. 13G',G'',H',H''), but they are of the same order as those produced by the measured PSF, PSF_2 (Fig. 13E',E''). A Zernike-polynomial-fitted version of the phase-retrieved PSF for PSF_1 was also tested and produced similar results to the two phase-retrieved PSFs (R -factor 0.0937; image not shown).

In contrast, a rotationally averaged version of PSF_1 (Fig. 13D) generated substantial image artefacts: there is significant residual intensity around the point-like objects (Fig. 13D') and alongside the crossed rods (Fig. 13D'') and the larger objects. An artefactual intensity asymmetry can also be discerned in

the inset cubes for the rotationally averaged and theoretical PSF deconvolution results (Fig. 13D,F), but is either not present or significantly weaker for the measured (Fig. 13C,E) or phase-retrieved (Fig. 13G,H) PSFs. These artefacts reflect the fact that the imaging properties of practical microscopes, like the one used here, are not in general perfectly rotationally symmetric, so they are not well represented by models that assume rotational symmetry. The final R -factor for this deconvolution was quite poor, 0.2954, more than twice that for the original, non-rotationally averaged PSF. The theoretical, ideal PSF suffers the same problem and produced similar artefacts, though its R -factor was lower, 0.1439. In general, the performance of phase-retrieved PSFs during image deconvolution was similar to that of measured PSFs, and better than that of strictly theoretical or measured but rotationally averaged PSFs.

Discussion and conclusions

Pupil functions provide a compact and modifiable description of microscope imaging properties, and phase retrieval provides a simple way to determine the pupil function of any microscope. The pupil function description combines advantages of measured and theoretical PSFs: it contains true, measured information about the particular microscope, but is also easily modified by calculated aberration functions. A pupil function directly displays aberration information about the system: one can quantitatively analyse its magnitude for attenuation effects and its phase for deviations from the optimal wavefront shape. Such deviations can be expressed in terms of classical aberrations, such as astigmatism, coma, etc., by expanding the pupil function in Zernike polynomials.

As a number of intensity PSF defocus sections are integrated to produce a single pupil function, the measurement noise present in the PSF is reduced in the pupil function, effectively by averaging. Artefacts in the measured PSF, such as dust shadows, that do not behave as expected for real PSF features as a function of defocus become similarly suppressed. The noise reduction reduces the need for rotational averaging, and thus allows rotational asymmetries to be described. Noise can be further reduced by fitting the pupil function to a parameterized model, such as a set of Zernike polynomials.

The pupil function is a very compact description of a microscope system: its size is effectively equivalent to merely two defocus sections of a measured intensity PSF. A 512×512 -pixel pupil function is merely 2 Mbytes – one-sixteenth the size of an intensity PSF containing 32 sections. Fitting the pupil function magnitude and phase into a set of 79 Zernike coefficients each results in an extraordinarily concise description of the microscope, occupying only 632 bytes. PSF calculation from a pupil function is quite fast: a 512×512 -pixel pupil function can be used to produce a 64-section PSF in 17.8 s on a 2.4-GHz Pentium IV processor.

Limitations of phase retrieval and pixelated pupil functions

The phase retrieval method described here is a very basic algorithm; many alternative algorithms have been developed in the astronomy literature (Paxman & Fienup, 1988; Fienup, 1993; Acton *et al.*, 1996; Lyon *et al.*, 1997; Luke *et al.*, 2002). Approaches exist in which Zernike coefficients are directly adjusted during phase retrieval (Lyon *et al.*, 1997). Most algorithms assume that the pupil function has constant magnitude over the pupil – an assumption that is valid for telescopes but not in general for microscopy – but there has been development to allow the magnitude to vary as well (Luke *et al.*, 2002). These algorithms could be modified to apply to microscopy, and may provide improved convergence and precision.

As used here, the phase-retrieved pupil function is a pixelated object, and some attention must be paid to its pixelation. The pixel density in the pupil plane is proportional to the lateral size of the PSF, which is usually determined by the measured PSF data. This pixel density will suffice to Nyquist-sample the defocus-related phase variations in the pupil function, as long as the real space image size fits the PSF laterally even at maximum defocus. It may not have enough margin left, however, also to catch the rapid phase variations that often occur in the pupil function itself, especially near its edge, due to lens imperfections. Another concern is the pupil edge itself, which is used to impose the NA constraint; coarse pixelation of the edge can generate artefactual ripples in the PSF. Such artefacts can be avoided by using a finer pixelation of the pupil function, if necessary by padding the PSF data laterally.

With the simple imaging model used in this article, the PSFs reconstructed from phase-retrieved pupil functions did not completely match the PSFs from the measured data. The difference was apparent in frequency space, where the pupil-function-derived OTFs showed a higher content of high spatial frequencies. Some but not all of this difference could be explained by taking into account vectorial effects and the finite size of the 'point source' used in the measurement. For the model to be completely satisfactory, the nature of the remaining difference in high-frequency content should be determined and the model refined accordingly; possible effects to investigate include chromatic and wavelength-dependent aberrations, and blurring due to mechanical vibrations. For the purposes of practical applications, however, empirical OTF rescaling as used here is sufficient to make PSFs calculated from phase-retrieved pupil functions match the measured PSF data quite closely. Thus pupil functions can already be used as a replacement for measured PSFs, for example in deconvolution algorithms.

Application of pupil functions in deconvolution

In biology, one often encounters imperfect imaging conditions during data collection, due to the properties of the sample not matching the requirements of the objective lens being used. The ability to combine theoretically calculated aberrations

with phase-retrieved pupil functions allows a single PSF measurement to be used to create a calculated PSF that is tailor-made to match any imaging conditions. This concept opens two major opportunities for image deconvolution in biology: pupil-function-based semi-blind deconvolution, and spatially dependent deconvolution. Blind deconvolution techniques (Holmes, 1992) could be designed to adjust a limited number of parameters of the pupil function, allowing a measured PSF to be tuned to the imaging conditions of the given dataset. The pupil function form, especially when parameterized, is much less redundant than a full 3D PSF, and therefore supplies strong constraints that should aid convergence of blind deconvolution methods.

In spatially dependent deconvolution, the PSF would be allowed to vary with position within the collected dataset (Hanser *et al.*, 2002). In the simplest form, the PSF would depend only on the depth into the sample; this situation is typical of index-mismatch aberrations and is very often encountered in practice. For this one would need a separate PSF for each axial section. Such a PSF series would be quite difficult to produce experimentally, but could easily be created by modifying a single measured pupil function with calculated aberration functions.

In conclusion, phase-retrieved pupil functions are an attractive way to quantify microscope imaging properties, and promise to play a major role in future processing developments.

Acknowledgements

This work was supported by the National Institutes of Health Grant GM-2510-24 (J.W.S.). B.M.H. acknowledges support from the Julius R. and Patricia A. Krevins, Lloyd M. Kozloff Fellowship at UCSF (2001-02). D.A.A. is a Howard Hughes Medical Institute Investigator.

References

- Acton, D.S., Soltau, D. & Schmidt, W. (1996) Full-field wavefront measurements with phase diversity. *Astron. Astrophys.* **309**, 661–672.
- Agard, D.A. (1984) Optical sectioning microscopy: cellular architecture in three dimensions. *Ann. Rev. Biophys. Bioeng.* **13**, 191–219.
- Agard, D.A., Hiraoka, Y., Shaw, P. & Sedat, J.W. (1989) Fluorescence microscopy in three dimensions. *Meth. Cell Biol.* **30**, 353–377.
- Beverage, J.L., Shack, R.V. & Descour, M.R. (2002) Measurement of the three-dimensional microscope point spread function using a Shack–Hartmann wavefront sensor. *J. Microsc.* **205**, 61–75.
- Booth, M.J., Neil, M.A.A. & Wilson, T. (1998) Aberration correction for confocal imaging in refractive-index-mismatched media. *J. Microsc.* **192**, 90–98.
- Fienup, J.R. (1993) Phase-retrieval algorithms for a complicated optical system. *Appl. Opt.* **32**, 1737–1746.
- Gibson, S.F. & Lanni, F. (1991) Experimental test of an analytical model of aberration in an oil-immersion objective lens used in three-dimensional light microscopy. *J. Opt. Soc. Am. A*, **8**, 1601–1613.
- Gonsalves, R.A. (1982) Phase retrieval and diversity in adaptive optics. *Opt. Eng.* **21**, 829–832.

- Goodman, J.W. (1968) *Introduction to Fourier Optics*, 2nd edn. McGraw-Hill, New York.
- Hanser, B.M., Gustafsson, M.G.L., Agard, D.A. & Sedat, J.W. (2001) Phase retrieval of widefield microscopy point spread function. *Proc. SPIE*, **4261**, 60–68.
- Hanser, B.M., Gustafsson, M.G.L., Agard, D.A. & Sedat, J.W. (2002) Application of phase retrieved pupil functions in wide-field fluorescence microscopy. *Proc. SPIE*, **4261**, 40–46.
- Hanser, B.M., Gustafsson, M.G.L., Agard, D.A. & Sedat, J.W. (2003) Phase retrieval for high numerical aperture optical systems. *Opt. Lett.* **28**, 801–803.
- Hecht, E. (1990) *Optics*, 2nd edn. Addison-Wesley, Reading, MA, pp. 94–102, 225–226.
- Hiraoka, Y., Sedat, J.W. & Agard, D.A. (1990) Determination of three-dimensional imaging properties of a light microscope system. *Biophys. J.* **57**, 325–333.
- Holmes, T.J. (1992) Blind deconvolution of quantum-limited incoherent imagery: maximum likelihood approach. *J. Opt. Soc. Am. A*, **9**, 1052–1061.
- Jackson, J.D. (1999) *Classical Electrodynamics*, 3rd edn. Wiley & Sons, New York, p. 411.
- Kam, Z., Hanser, B., Gustafsson, M.G.L., Agard, D.A. & Sedat, J.W. (2001) Computational adaptive optics for live three-dimensional biological imaging. *Proc. Natl Acad. Sci. USA*, **98**, 3790.
- Luke, D.R., Burke, J.V. & Lyon, R.G. (2002) Optical wavefront reconstruction: theory and numerical methods. *SIAM Rev.* **44**, 169–224.
- Lyon, R.G., Dorband, J.E. & Hollis, J.M. (1997) Hubble Space Telescope Faint Object Camera calculated point spread functions. *Appl. Opt.* **36**, 1752–1765.
- Mahajan, V.K. (1994) Zernike circle polynomials and optical aberrations of systems with circular pupils. *Appl. Opt. Suppl.*, 8121–8124.
- McCutchen, C.W. (1964) Generalized aperture and the three-dimensional diffraction image. *J. Opt. Soc. Am.* **54**, 240–244.
- Neil, M.A.A. & Booth, M.J. & Wilson, T. (1998) Dynamic wave-front generation for the characterization and testing of optical systems. *Opt. Lett.* **23**, 1849–1851.
- Noll, R. (1976) Zernike polynomials and atmospheric turbulence. *J. Opt. Soc. Am.* **66**, 207–211.
- Paxman, R.G. & Fienup, J.R. (1988) Optical misalignment sensing and image reconstruction using phase diversity. *J. Opt. Soc. Am. A*, **5**, 914–923.
- Philip, J. (1999) Optical transfer function in three dimensions for a large numerical aperture. *J. Mod. Opt.* **46**, 1031–1042.
- Richards, B. & Wolf, E. (1959) Electromagnetic diffraction in optical systems II. Structure of the image field in an aplanatic system. *Proc. Roy. Soc. London, Series A*, **253**, 358–379.
- Scalettar, B.A., Swedlow, J.R., Sedat, J.W. & Agard, D.A. (1996) Dispersion, aberration and deconvolution in multi-wavelength fluorescent images. *J. Microsc.* **182**, 50–60.
- Sheppard, C.J.R. & Torok, P. (1997) Effects of specimen refractive index on confocal imaging. *J. Microsc.* **185**, 366–374.
- Török, P., Varga, P. & Németh, G. (1995) Analytical solution of the diffraction integrals and interpretation of wave-front distortion when light is focused through a planar interface between materials of mismatched refractive indices. *J. Opt. Soc. Am. A*, **12**, 2660–2671.
- Visser, T.D. & Wiersma, S.H. (1991) Spherical aberration and the electromagnetic field in high-aperture systems. *J. Opt. Soc. Am. A*, **8**, 1404–1410.
- Zhou, H. & Sheppard, C.J.R. (1997) Aberration measurement in confocal microscopy: phase retrieval from a single intensity measurement. *J. Mod. Opt.* **44**, 1553–1562.